

GT2012-69306

# DRAFT: COMPUTATIONAL VALIDATION OF THE FLOW THROUGH A TURBINE STAGE AND THE EFFECTS OF RIM SEAL CAVITY LEAKAGE ON SECONDARY FLOWS

Özhan H. Turgut\*

Turbomachinery Aero-Heat Transfer Laboratory  
Department Aerospace Engineering  
The Pennsylvania State University  
University Park, Pennsylvania 16802  
Email: oht101@psu.edu

Cengiz Camci†

Turbomachinery Aero-Heat Transfer Laboratory  
Department Aerospace Engineering  
The Pennsylvania State University  
University Park, Pennsylvania 16802  
Email: cxc11@psu.edu

## ABSTRACT

A computational validation study related to aerodynamic loss generation mechanisms is performed in an axial flow turbine. The 91.66 cm diameter axial flow turbine research facility has a stationary nozzle guide vane assembly and a 29 bladed HP turbine rotor. The NGV inlet and exit Reynolds numbers based on midspan axial chord are around 300000 and 900000, respectively. GRIDPRO is used as the structured grid generator.  $y^+$  values are kept below unity. The finite-volume flow solver ANSYS CFX with SST  $k - \omega$  turbulence model together with the transitional flow model is employed. Experimental flow conditions are imposed at the boundaries. The computational predictions are compared to experimental data at NGV exit plane and rotor inlet plane. NGV exit plane measurements come from a previous experimental study with a five-hole probe and the data at rotor inlet plane is taken by the current authors using a Kiel probe with 3.175mm head diameter. The comparison of rotor-stator interface models shows that the stage model, which calculates the circumferentially averaged fluxes and uses as the boundary condition at the interface plane, agrees well with the experimental total pressure coefficient data at the NGV exit. The difference between the NGV only simulation and the rotor-stator simulation is emphasized. The effect of rim seal flow on the mainstream aerodynamics is investigated. This validation study shows that the effect of future geometrical modifications on the endwalls and

the vane will be predicted reasonably accurately.

## NOMENCLATURE

- $c$  Midspan axial chord length of nozzle guide vane.
- $C_p$  Pressure coefficient;  $(P_1 - P_2)/(0.5 \rho U_m^2)$ .
- $C_{Pt}$  Total pressure coefficient;  $(P_{03} - P_{01})/(0.5 \rho V_1^2)$ .
- $C_{Pt}'$  Total pressure coefficient;  $(P_{02} - P_{01})/(0.5 \rho U_m^2)$ .
- $P$  Static pressure.
- $P_0$  Total pressure.
- $Re_{\theta_t}$  Momentum-thickness Reynolds number.
- $T_0$  Total temperature.
- $U_m$  Blade speed at mean radius.
- $V$  Velocity magnitude.
- $V_x$  Axial velocity component.
- $V_r$  Radial velocity component.
- $V_\theta$  Circumferential velocity component.
- $x$  Axial distance from nozzle guide vane leading edge.
- $y^+$  Non-dimensional wall coordinate;  $\frac{\sqrt{\tau_w/\rho} \cdot y_p}{\nu}$ .
- $y_p$  First grid height off the wall.

## Greek

- $\gamma$  Intermittency.
- $\nu$  Kinematic viscosity.
- $\rho$  Density.
- $\tau_w$  Wall shear stress.
- $\omega$  Turbulent frequency.

## Subscripts

\*Graduate Research Assistant, ASME Student Member

†Professor of Aerospace Engineering, ASME Fellow

- 1 One axial chord upstream of nozzle guide vane leading edge.
- 2 Nozzle guide vane exit plane,  $x/c = 1.025$  from midspan trailing edge.
- 3 Rotor inlet plane,  $x/c = 1.018$  from casing trailing edge.

#### Abbreviations

- N Turbine nozzle guide vane.  
 R Turbine blade.  
 SST Shear stress transport.  
 TKE Turbulence kinetic energy.

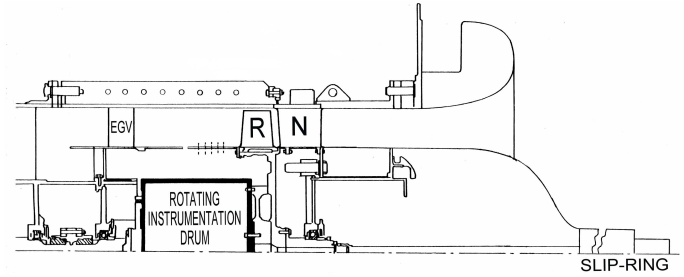


**FIGURE 1:** The turbine facility sketch.

## INTRODUCTION

One of the important flow phenomena in axial flow turbine aerodynamics is the flow ingestion from the mainstream to the cavity between the vane and the rotor row. It is crucial to prevent this hot gas penetration to the wheelspace for structural integrity, which may be adversely affected by the overheating of the materials. To restrain this ingestion, coolant flow is purged through this wheelspace. But the interaction of this coolant air with the mainstream introduces extra loss and reduces the turbine efficiency. So, the amount of purge flow should be carefully adjusted.

The hot gas flow coming through the nozzle guide vane passage tend to ingress this cavity due to a few reasons as discussed in [1]. One important reason is because of the rotor pumping effect. As the rotor spins, the centrifugal acceleration forces the boundary layer fluid move in the radially outward direction. And if the amount of this flow is greater than the purge flow supplied, then to account for the mass imbalance, the hot mainstream flow ingress to this cavity. The second main reason for flow ingestion is the circumferential static pressure nonuniformities at the vane exit. This circumferential variation is mainly associated with the rotor-stator interaction which may lead to an increase in static pressure locally. If the static pressure of the hot gas flow is greater than the one in the seal, then the ingestion occurs.

Many researchers have studied rim seal flow ingestion [1–9]. The aerodynamics and the heat transfer aspects of this hot gas flow ingestion have been investigated both experimentally and numerically. More emphasis was given to the effects of this ingestion. However, it is also important to study influence of the rim seal purge flow on the mainstream. The studies involving the effect of leakage flow on external mainstream are summarized below.

The influence of rim seal cavity flow on the mainstream was studied Hunter and Manwaring [10]. They performed experimental and numerical investigation on a two stage low speed research turbine. They found that the rim seal cavity related loss was due to the mixing of circumferential momentum components. The effect of the seal flow after the first stator was seen in the first rotor and second stator passages.

McLean et al. [11, 12] measured the effects of wheelspace coolant injection in an axial turbine research facility. The study

involved the experimental data taken both in stationary and rotational frame of reference. They have tested three different types of coolant flow injections, namely radial, impingement, and root injection cooling. Measurements taken in the stationary frame showed that the root injection cooling reduced the overturning and underturning. Radial and impingement injection made the boundary layer thicker, and hence, shifted the velocity profiles radially outward. In terms of the total-to-total efficiency, 1% root injection cooling increased the efficiency by 1.5% near the blade midspan. In their following paper, the rotational domain measurements showed that due to the passage vortices, the cooling injection effects are seen at the midspan. They concluded that the cooling has large influence on the rotor inlet boundary layers and secondary flows.

The interaction of the turbine passage flow and the cavity flow between rotor and stator was analyzed by Paniagua et al. [13]. They performed experimental investigation in a transonic high-pressure turbine stage. Three-dimensional Navier-Stokes computational evaluation was compared with the measured data. Time-averaged measurements at the vane exit showed an increase in the static pressure when there is a 1.5% ejection from the cavity. It was observed at the vane exit that the time-resolved static pressure fluctuations are reduced. The rotor hub passage vortex moved radially outward with an increased intensity. The total pressure loss was increased between 5% and 30% span at the stage exit.

Another study on the interaction of vane passage flow near hub and the rim cavity flow was investigated experimentally by Gallier et al. [14]. They used a Particle Image Velocimetry (PIV) technique on the first stage of their research turbine. The authors tested two different seal mass flow rates. The lower flow rate had little effect on secondary flow and also led to flow ingestion at the rim seal cavity. To prevent this ingestion, higher seal mass flow rate was used which increased the horseshoe vortex size. The wake of the vane changed the seal flow in a positive way such that it decreased the radial growth of the seal flow.

Ong et al. [15] performed experimental measurements and computational evaluation to see the effects of coolant injection on the mainstream of a high-pressure turbine stage. They in-

**TABLE 1:** The AFTRF design performance parameters.

Inlet Total Temperature ( $^{\circ}K$ ); $T_{01}$	289
Inlet Total Pressure ( $kPa$ ); $P_{01}$	101.36
Mass Flow Rate ( $kg/s$ ); $\dot{Q}$	11.05
Rotational speed (rpm); $N$	1300
Total Pressure Ratio; $P_{01}/P_{03}$	1.0778
Total Temperature Ratio; $T_{03}/T_{01}$	0.981
Pressure Drop ( $mmHg$ ); $P_{01} - P_{03}$	56.04
Power ( $kW$ ); $P$	60.6

investigated the interaction between the hub leakage flow and the rotor secondary flow. They found that 1.33% leakage mass flow increased the penetration depth of the secondary flow by 9.5% span in experiments and 7% span in CFD. An engine representative stage was simulated and the higher leakage mass flow rate raised the penetration depth. The authors further studied the swirl effect on the secondary flows. It was found that as the swirl angle was increased, the penetration depth was reduced. It also increased the stage efficiency by 0.75%.

Reid et al. [16] studied seal flow effects on mainstream of an axial turbine both experimentally and numerically. They tested various seal mass flow rates and found that higher seal mass flows resulted in a decrease in efficiency. But this efficiency loss would be decreased with higher tangential velocity of the sealant flow. It was concluded that the seal flow had a strong influence on the mainstream tangential velocity.

The interaction of the secondary flows with the purge flow was investigated experimentally by Schuepbach et al. [17]. They used two different mass flow rates of -0.14% indicating a suction and a blowing of 0.9% in a one-and-1/2-stage axial turbine. They found that the difference of changing the flow rate from -0.14% to 0.9% decreased the total-to-total efficiency by 0.6%. They also observed that the seal flow was entrained by the hub secondary flow.

The effect of rim seal flow on the secondary flow structures of an axial turbine was studied by Schuepbach et al. [18]. They presented experimental and computational results of two different nonaxisymmetric contoured endwalls and the axisymmetric baseline cases for a one-and-1/2-stage high work axial turbine. They tried two seal flow configurations, -0.1% injection rate as suction and 0.9% injection rate as blowing. Experimental measurements showed that the efficiency gains due to the nonaxisymmetric endwalls decrease as the seal flow mode changes from suction to blowing.

**TABLE 2:** The AFTRF design features.

Rotor Hub Tip Ratio	0.7269
Tip Radius ( $m$ ); $R_{tip}$	0.4582
Blade Height ( $m$ ); $h$	0.1229
Tip Relative Mach Number	0.24 (max)
Nozzle Guide Vane (tip)	
number	23
chord ( $m$ )	0.1768
spacing ( $m$ )	0.1308
turning angle	70
maximum thickness ( $mm$ )	38.81
Midspan Axial Chord	
nozzle ( $m$ )	0.1123
rotor ( $m$ )	0.09294
Vane Reynolds Number	
based on inlet velocity	$(3 \sim 4) \times 10^5$
based on exit velocity	$(9 \sim 10) \times 10^5$

This paper is the continuation of the previous work of Turgut and Camcı [19]. The former validation study included Nozzle Guide Vane (NGV) only simulation. The effects of rotating turbine blades aft of the NGV and the rim seal leakage flow between NGV and rotor row was neglected. However, in an aerodynamic validation study of an axial flow turbine stage, it is essential to include these effects in order to get reasonable approximation to the actual operating conditions. In the following sections, the Axial Flow Turbine Research Facility (AFTRF) and the measuring method is introduced and the computational simulation details is discussed. The experimental and computational results of total pressure coefficient between the NGV and the rotor will be presented. The influence of rotating domain is emphasized, and in addition, the rim seal flow is included in the simulation and the corresponding results will be discussed.

## EXPERIMENTAL FACILITY

The Axial Flow Turbine Research Facility (AFTRF) is installed at the Turbomachinery Aero-Heat Transfer Laboratory of the Pennsylvania State University. The AFTRF is a low speed, single-stage, cold flow turbine having a diameter of 91.66 *cm*.

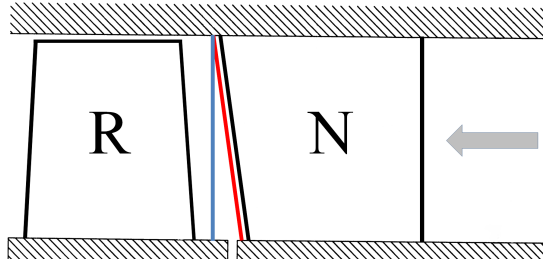


**FIGURE 2:** Rotor inlet plane perpendicular to axial direction and NGV exit plane parallel to NGV trailing edge.

Table 1 summarizes the design performance parameters of the turbine facility and the features are shown in Tab. 2. The detailed description and the characteristics of the AFTRF can be found from Camcı [20]. The facility is driven by four axial suction fans downstream of the rotor section and the speed of the rotor is controlled by a power absorbing eddy-current brake. Inlet has a bell-mouth shape followed by the NGV row and the rotor blades. A sketch of the AFTRF is given in Fig. 1. There are 23 NGV's and 29 rotor blades followed by the exit guide vanes.

Figure 2 shows the two planes where the experimental data is measured. The first plane, *NGV Exit Plane*, is parallel to the NGV trailing edge line and it is located at  $x/c = 1.025$  from the NGV trailing edge at midspan. The measurements at this plane was taken by previous researchers and the detailed information can be found in [21]. The second experimental plane, *Rotor Inlet Plane*, is perpendicular to the axial flow direction and it is located at  $x/c = 1.018$  from the NGV trailing edge at casing. The authors of this study completed the total pressure measurements at this rotor inlet plane, which is at the downstream of the rim seal cavity. The radial traversing starts at %5 of the vane span. It is also found that above %35 of the span, the variations in measurements are minimal. Therefore, the maximum location in radial direction is selected as %38 of the span, which helped in reducing the time needed for a complete measurement of one pitch in circumferential direction.

The total pressure measurements at the rotor inlet plane are carried out by a Kiel probe manufactured by United Sensor Corporation [22]. The probe has a  $3.175\text{mm}$  ( $0.125\text{in.}$ ) head diameter. The main advantage of Kiel probe is the extensive range of insensitivity to yaw and pitch angles. The manufacturer documents the ranges as  $\pm 48^\circ$  and  $\pm 45^\circ$  for yaw and pitch, respectively. Before the experiments, probe is manually aligned with the NGV exit flow design angle, which is  $70^\circ$  from the axial direction. Zaccaria and Lakshminarayana [21] reported that the flow yaw and pitch angles deviate from design value within  $\pm 5^\circ$ . The probe is mounted on a single-axis linear traverser which moves in radial direction. This linear traverser is installed on a circumferential traverser that is attached to the facility window.

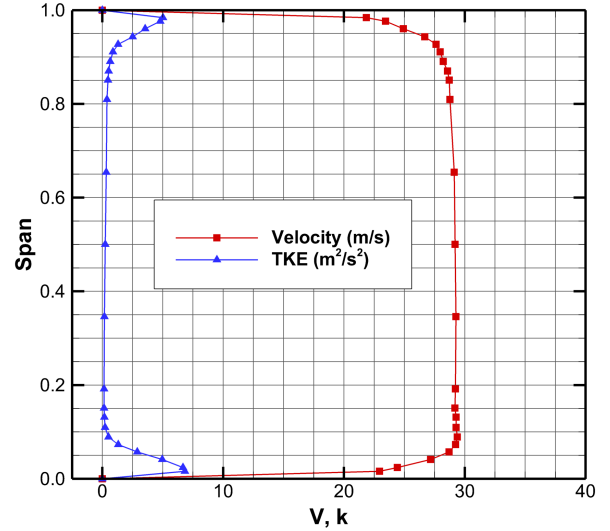


**FIGURE 3:** Experimental inlet velocity magnitude and turbulent kinetic energy distribution.

The slot on the window allows the circumferential traversing mechanism to complete 1.5 vane pitch. But, authors decided to traverse one full pitch in circumferential direction for time considerations. There are 18 radial and 25 circumferential locations that the probe collects data, which makes 450 data points.

Kiel probe is connected to a pressure transducer, and the analog data from the transducer is transferred to a 12 bit data acquisition (DAQ) board. A computer program is developed using commercial software LabView which reads the data coming from DAQ and performs necessary calculations and exports the  $C_{Pt}$  values. The estimated uncertainty in  $C_{Pt}$  is 0.6%.

## COMPUTATIONAL FEATURES

The simulations in this paper is carried out by the commercial finite-volume flow solver ANSYS CFX. The three-dimensional compressible RANS flow equations are solved for steady and unsteady air flow through a turbine stage. Rotationally periodic boundary conditions are applied on the side walls of the computational domain. No-slip, adiabatic wall is selected for vane, hub and casing boundaries. For the inlet boundary, experimental flow conditions measured at one axial chord upstream of the NGV are adapted [23]. The velocity magnitude and the turbulent kinetic energy distribution along the span at the inlet is shown in Fig. 3. The total pressure value is given at the inlet boundary condition which is extracted from the velocity distribution. Total temperature at the inlet is  $298.15\text{ K}$ . At the outlet boundary, experimental mass flow rate value is specified.

The interface plane between the stationary and rotating do-

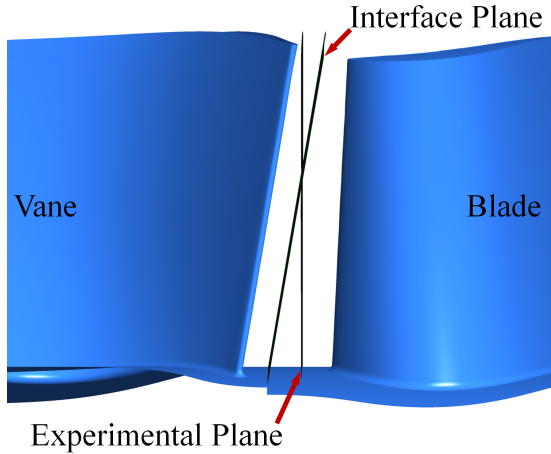


**FIGURE 4:** Interface plane between NGV and rotor row.

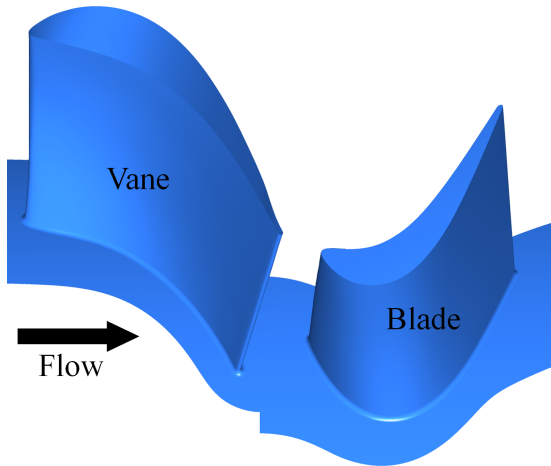


**FIGURE 5:** Frozen rotor location of the simulation.

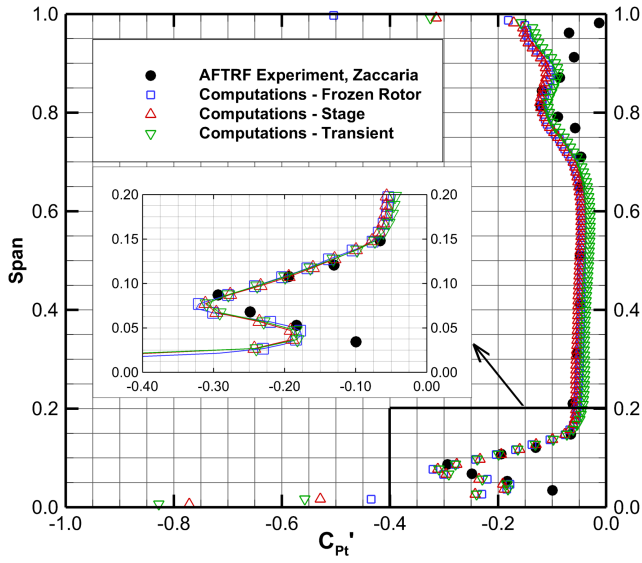
main is shown in Fig. 4. It is parallel to the NGV trailing edge. Note that, the intersection plane and the rotor inlet experimental plane intersects around 60% span. In other words, rotor inlet plane has two parts, one in stationary and the other in rotating domain. This does not cause any problem in comparing the computational results with the experimental measurements since the comparison will be made between 5% and 38% vane span.

ANSYS CFX has three types of rotor-stator interface definitions, namely frozen rotor, stage, and transient rotor-stator. *Frozen rotor* model gives a steady state solution for fixed relative positions of the domains. It calculates the flow parameters going from one domain to the other by taking into account the frame of reference. If there is a pitch change between the components, the fluxes at the interface are scaled according to this pitch ratio. This

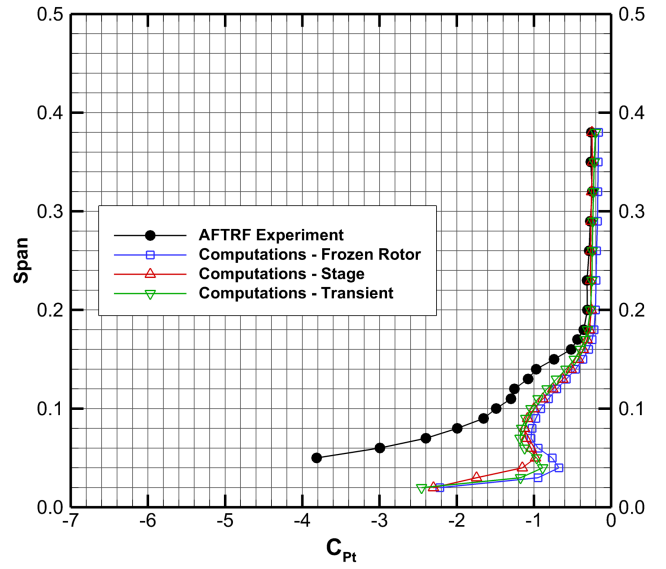
model needs the least computational time and sources among the three different interface models, but on the other hand, it does not have the transient effects of the rotor-stator simulation. The fixed relative positions of the NGV and the rotor in this study is shown in Fig 5. *Stage* model is the other steady state simulation approach. Unlike the frozen rotor approach which simulates the fixed positions of the domains, this model calculates circumferentially averaged fluxes at the interface plane on various radial bands. These averaged values are then used as inflow boundary condition for the other component. This method allows a simulation of a time averaged rotor-stator interaction, but still, stage model lacks the transient effects. *Transient rotor-stator* model uses a sliding interface to account for the transient interaction between the rotor and the stator. It calculates the flow parameters according to the relative motion of the components. The pitch change between the stator and rotor domain is important in transient model. This model requires a pitch ratio close to unity for accurate predictions. The main disadvantage of this model is the computational requirements for the transient data calculation and storage.

The axial turbine research facility, AFTRF, has 29 rotor blades and 23 vanes, as mentioned earlier. This unequal number of blades indicates that the pitch ratio between the components is approximately 1.25. For the pitchwise periodic boundary conditions at the interface plane, this unequal blade count might introduce simulation errors. In order to achieve the most accurate predictions for a turbomachinery unsteady flow simulation, one has to include all the vanes and the rotors in the computational environment. Obviously, this is not a practical way in terms of computational efficiency. Therefore, previous researchers have tried different methods to account for the unequal number of blades. One way is to use one-to-one vane/blade ratio. This is accomplished by means of scaling the blade as shown in Michalessi et al. [24], Ameri et al. [25], and Dawes [26]. Ameri et al. [27] reported that in terms of heat transfer calculations, 1:1 and 2:3 vane/blade ratios gave the same average values. Abhari et al. [28] performed 2D simulation with space-time coordinate transformation for the arbitrary pitch ratios. Phase lagged boundary conditions were used at the interface by He and Denton [29], Gerolymos et al [30], Van Zante et al. [31], Shyam et al. [32]. Another method is the time-inclining technique studied by Giles [33], Jung et al. [34], and Zhou et al. [35].

The authors of this paper followed two ways. First way is to use one-to-one blade count ratio, which involves rotor blade scaling. The other one is to implement 4 vanes and 5 blades in the simulation to get the pitch ratio closer to unity. Note that, simulating 4 vanes and 5 blades involves nearly 12 million mesh elements, and requires huge computer resources and time. These methods are compared to each other based on the total pressure coefficient distribution. The figures are shown in the Appendix. It is clear from these figures that scaling the rotor blades did not introduce extra loss between the stationary and the rotating do-



(a) NGV exit plane, compared with experimental data [21]



(b) Rotor inlet plane

**FIGURE 6:** Effect of various rotor simulation types in total pressure coefficient.

main. The results coming from two different methods are almost the same. After this conclusion, the authors decided to use blade scaling technique for computational resources and time considerations.

Menter's [36] two-equation eddy-viscosity model gives good predictions especially when there is an adverse pressure gradient in the boundary layer. This shear stress transport (SST) model is based on  $k-\omega$  turbulence closure formulation. Also, the flow through an NGV passage is transitional, and one should account for the transition effects as discussed in [19]. One of the methods to predict the transition is the Gamma Theta model in CFX. This model is based on an empirical correlation and two more transport equations are solved; one for the momentum thickness Reynolds number ( $Re_{\theta t}$ ), and the other for the intermittency ( $\gamma$ ). This model is validated for various transitional flows together with SST turbulence model.

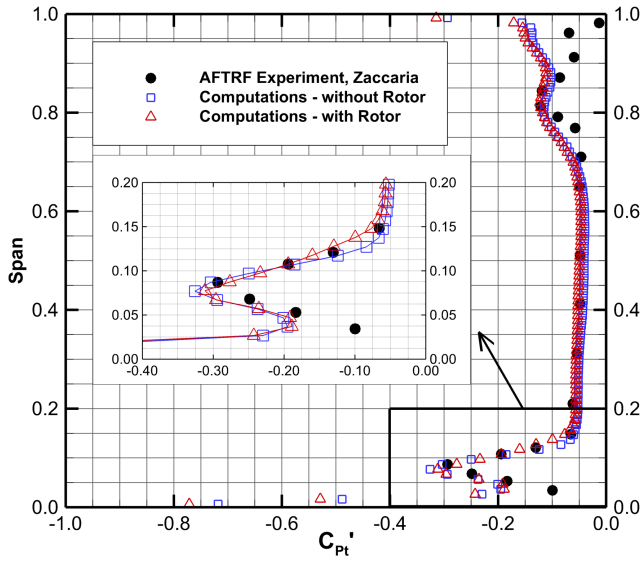
Based on the discussion and the results presented in [19], the authors applied structured mesh to represent the flow field. Three-dimensional computational mesh is created by GRIDPRO. Multi-block, body-fitted structured grid gives more reasonable flow predictions in comparison to unstructured grid, even though unstructured mesh is easy and quicker to implement for complex geometrical designs. Since the near-wall grid resolution is the key for transitional flows and for capturing the secondary flow formation, the non-dimensional wall distance of  $y^+ < 1$  is satisfied everywhere in the domain. NGV domain has 1 million and rotor domain has 1.5 million hexahedral cells.

## RESULTS AND DISCUSSION

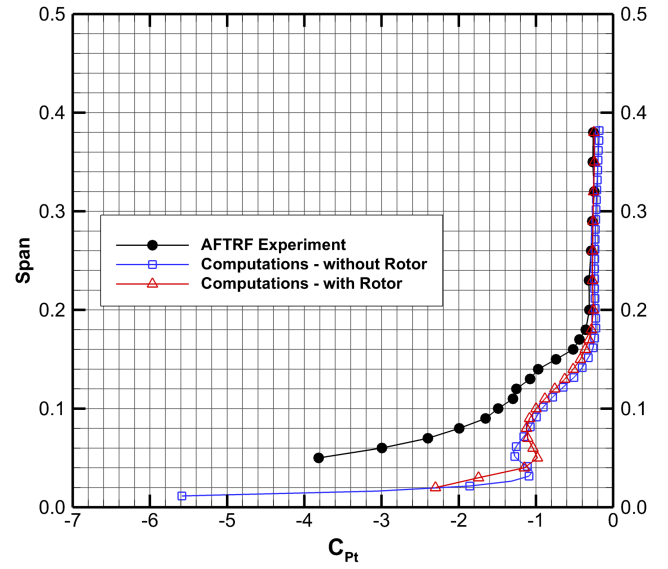
As mentioned in the previous section, there are three interface models in CFX at the stationary and rotating domain interface. Frozen rotor and stage calculations are steady state flow approximations and have rotor-stator interaction. Frozen rotor simulation is for a fixed position of the rotor and has the results for that specific position only. On the other hand, stage calculation uses the circumferentially averaged parameters at the rotor-stator interface plane, and has time average interaction effects. The transient rotor-stator interface model include the unsteady effects, and therefore the time-averaged values are presented in the results. In the transient simulation, rotor blade moves one blade pitch in 20 timesteps. The authors found that 20 timesteps is sufficient for capturing the transient effects.

Figures 6a and 6b show the total pressure coefficient distribution along the span for different rotor-stator simulation interface models. At the NGV exit plane, shown in Fig. 6a, three interface models predict in accordance to each other, especially in the hub secondary flow region. The computations overestimate the peak value of  $C_{Pt}'$  by 7% near the 7.5% span. The time-averaged transient computation predicts a lower profile loss above 17% span compared to experimental data and the other two interface types. There is a difference of  $\Delta C_{Pt}' = 0.1$  which is approximately 170Pa. However, the time-averaged transient simulation results are in good agreement with the experimental profile loss at the rotor inlet plane, as shown in Fig. 6b. Note that, the definitions of total pressure coefficients are different for Figs. 6a and 6b.  $C_{Pt}'$  is normalized by the rotor midspan speed





(a) NGV exit plane, compared with experimental data [21]



(b) Rotor inlet plane

**FIGURE 7:** The comparison of total pressure coefficient with and without rotor simulation.

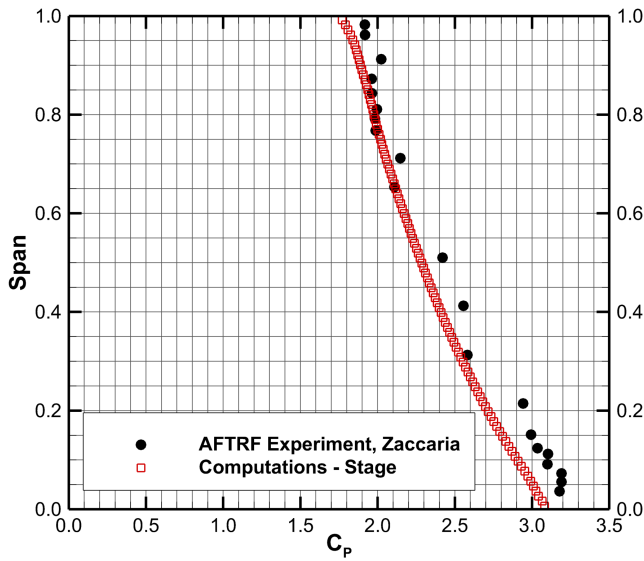
as described in [21], whereas  $C_{Pt}$  is normalized by the midspan inlet velocity. This inconsistency in profile loss predictions in transient rotor-stator simulation may be interpreted as the effect of blade passing in the upstream direction might not be properly transformed to the stationary domain. It is clear from Fig. 6b that the underprediction of profile loss in frozen rotor calculation is due to the fixed position of the rotor and the profile loss is calculated for that position of the rotor. Below 20% span, the computational results of all interface models deviate from the experimental data. This observation will be discussed in the following paragraphs.

The comparison between these three different rotor-stator interface models tells that stage calculations will be as accurate as the transient simulation, and with less computational resource and time requirements. Although the frozen rotor approach needs the least time to run a simulation, the main drawback is that it represents the aerodynamics of only one specific position of the rotor. Therefore, the authors of this paper decided to use stage interface model in the further computations.

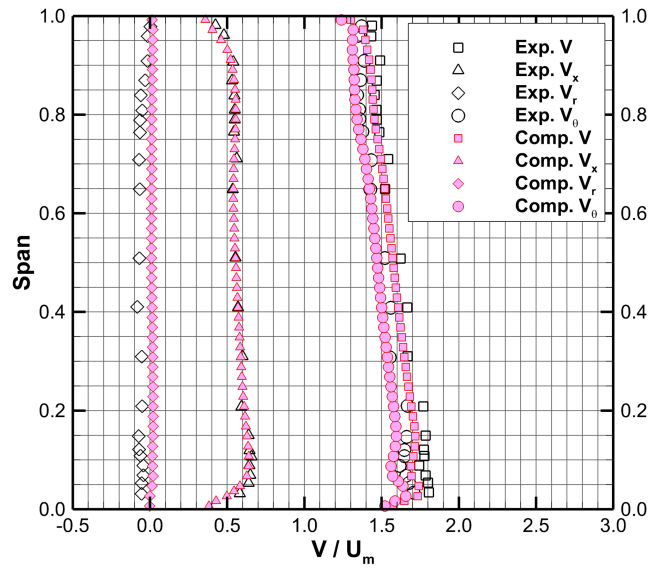
The numerical validation of the AFTRF nozzle guide vane aerodynamic experiments was reported by Turgut and Camcı [19]. In that paper, the authors did not include the rotating domain in the computations, and hence, the rotor-stator interaction was not involved. In the present study, one of the goals is to investigate the aerodynamic influence of rotating domain aft of the nozzle guide vane row. The details of the CFD simulation was described in the previous sections. Figures 7a and 7b present the influence of rotor existence in total pressure coefficient distribu-

tion at the NGV exit plane and rotor inlet plane, respectively. The  $C_{Pt}'$  distribution in Fig. 7a tells that including the rotating domain in the simulation does not alter the results significantly above 16% span at the NGV exit plane. The peak value of  $C_{Pt}'$  decreases 6% when the rotor is introduced. The location of the secondary flow area remains unchanged. On the other hand, at the rotor inlet plane, the secondary flow moves radially outward, as shown in Fig. 7b. NGV only computations predict this lossy region around 5.5% span, whereas rotor existence pushes it up in spanwise direction to 8% span. Likewise, the peak value of  $C_{Pt}$  decreases by 13% with the addition of the rotating domain. This decrease conforms the NGV exit plane results, except the magnitude of reduction. But, one has to keep in mind that the definitions of total pressure coefficients are different at these measurement planes. It is observed from the experimental measurements in Fig. 7b that the secondary flow coalesce with the end-wall boundary layer. But still, there is a distinct secondary flow feature observed near 12% span in the experimental measurements. The computation predicts the profile loss accurately, but, it fails to estimate the experimental  $C_{Pt}$  data especially in the secondary flow area and the endwall boundary layer. Although the involvement of rotor in the computations helped to shift the lossy region radially upwards, there is still a difference in the location of the secondary flow and the magnitude of the total pressure losses.

The static pressure coefficient and the velocity components distributions are shown in Figs. 8a and 8b, respectively. The static pressure coefficient agrees well with the experimental data



(a) Pressure coefficient



(b) Velocity components

**FIGURE 8:** The distribution of pressure coefficient and velocity components at NGV exit plane with rotor simulation, comparison with experimental data [21].

except below 30% span.  $C_p$  decreases by 6% near the hub end-wall, which tells from the definition that the static pressure rises at that region. Similarly, the circumferential velocity component deviates from the experimental data by approximately 4% below 30% span. This decrease in velocity is consistent with the increase in static pressure, since the total pressure component remains nearly unchanged. As the dominating velocity component is the circumferential one, there is also a mismatch in velocity magnitude distribution.

It is clear from Fig. 7b that the mismatch between the simulation and the experimental data indicates another physical influence which shifts the endwall boundary layer and the secondary flow in the upwise direction along the span. The authors think that this may be due to the flow coming from the seal between NGV and blade rows. The rotation of the rig creates a pumping effect which pushes the airflow radially outward, which in turn, mixes with the flow coming through the NGV passages. In order to get a reasonable computational prediction of the experimental measurements, it is necessary to include this seal flow in the simulation. The seal flow location (red zone) and the interface plane (green inclined plane) between stationary and rotating domains are illustrated in Fig. 9. The seal is exactly at the same location as in the experimental facility AFTRF, and it has a width of 2mm. For computational ease, rim seal flow is treated as another inlet boundary condition with an imposed mass flow rate. As seen from this figure that seal inlet is a cylindrical surface and the flow is perpendicular to this inlet boundary.

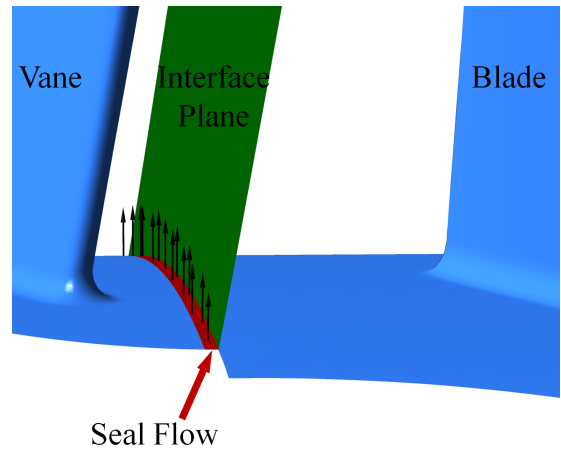
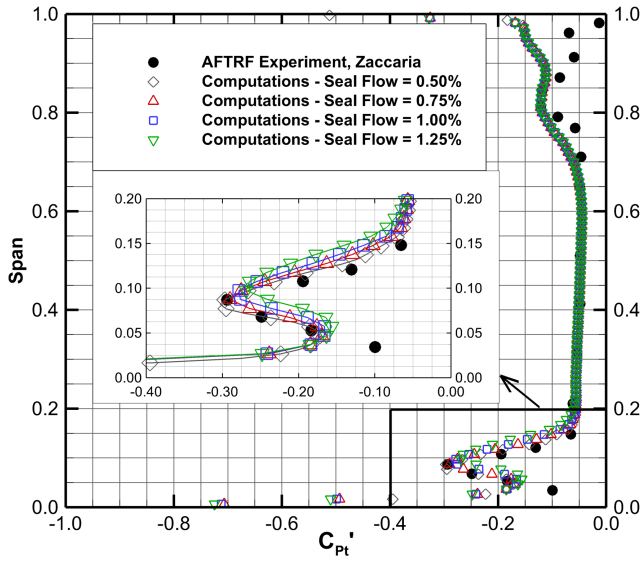


**FIGURE 9:** Rim seal location.

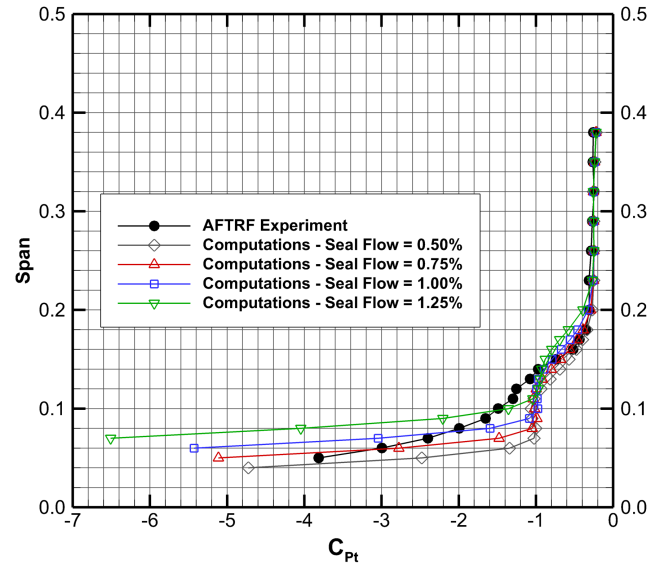
The exact amount of flow coming through the seal between the NGV and rotor row is not measured, therefore it is not known. The authors decided to perform computational tests with different mass flow rates for better quantification of this seal flow and in turn for accurate predictions. Four different percentages of NGV inlet mass flow rate are examined, namely 0.50%, 0.75%, 1.00%, and 1.25%.

The total pressure coefficient distribution along the span at





(a) NGV exit plane, compared with experimental data [21]



(b) Rotor inlet plane

**FIGURE 10:** Effect of rim seal mass flow rate percentage in total pressure coefficient.

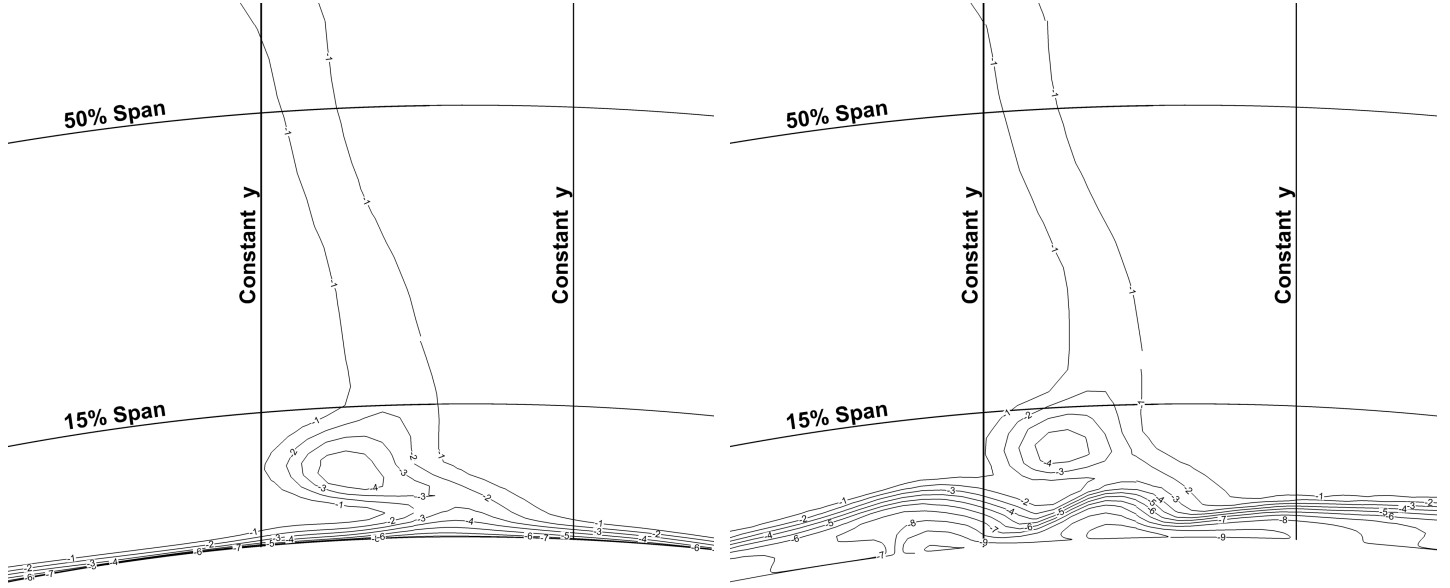
NGV exit and rotor inlet plane are shown in Fig. 10. The distribution at NGV exit plane (shown in Fig. 10a) tells that as the percentage of seal flow increases, the secondary flow rises in the radially outward direction. For instance, the peak value of  $C_{Pt}'$  lies around 8% span for 0.50% mass flow rate, whereas for 1.25% mass flow rate, this location is at 10% span. Another important observation is that the magnitude of the peak value of this secondary flow structure is inversely related to the mass flow rate. As the mass flow rate increases from 0.50% to 1.25%, the  $C_{Pt}'$  magnitude decreases from -0.3 to -0.27, showing a 10% reduction in total pressure loss. Mass flow rates of 0.50% and 0.75% give reasonably accurate  $C_{Pt}'$  predictions around secondary flow region when compared to experimental data. Above 20% span, all four mass flow rates estimate closer  $C_{Pt}'$  values, indicating that these specific mass flow rates do not change the distribution above this span location. Also note that, the profile loss is accurately predicted.

The seal flow has a similar effect on downstream as in the upstream flow.  $C_{Pt}$  distribution at the rotor inlet plane is depicted in Fig. 10b. Similar to the discussion in the previous paragraph, as the mass flow rate increases, the  $C_{Pt}$  levels shift in spanwise direction. A fixed value of  $C_{Pt} = -3$  is estimated at 5, 6, 7, and 8.2% span locations for mass flow rates of 0.50%, 0.75%, 1.00%, and 1.25%, respectively. Another way of discussing this result is that for these flow rates at 7% span, the predicted  $C_{Pt}$  values are -1, -1.5, -3, and -6.5, respectively. Clearly, the mixing of upstream fluid with the seal flow introduces an extra total pressure loss. Also, the endwall boundary layer gets thicker with

the increased seal mass flow rate. 0.75% seal flow calculates the secondary flow region accurately near 12% span, similar to experimental measurements. Moreover, it also estimates the total pressure coefficient near the hub endwall more precise than the other three flow rates. The authors thought 0.75% mass flow rate for the rim seal flow has an acceptable accuracy when compared to experimental data taken at AFTRF.

The equal  $C_{Pt}$  contour lines at the rotor inlet plane present the influence of rim seal flow, as shown in Fig. 11. These contour lines are extracted from a frozen rotor simulation with a 0.75% mass flow rate seal flow. The reason for using frozen rotor is that the stage interface model uses the circumferentially averaged values at the inlet boundary of the rotating domain. Therefore, all the local flow features are smeared out. One has to use either frozen rotor model or transient rotor-stator approach to get distinct local variances. The comparison between Figs. 11a and 11b tell that when the seal flow is introduced, the secondary flow location moves radially outward from 8% to 11% span. This observation agrees well with [11–13]. On the other hand, it has nearly the same  $C_{Pt}$  magnitude in the core of the secondary flow. Another important observation is the hub endwall boundary layer occupies 6% span, which is four times taller than the case without seal flow with 1.5% boundary layer thickness. The wake of the NGV is nearly unaltered.

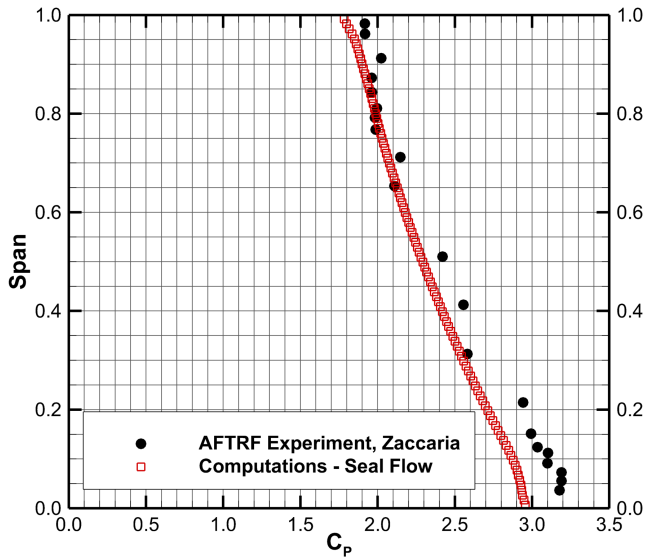
The static pressure coefficient and the velocity component distributions are shown in Figs. 12a and 12b, respectively. Similar to the results of rotor-stator simulation without the seal flow, there is a mismatch with the experimental data both in static pres-



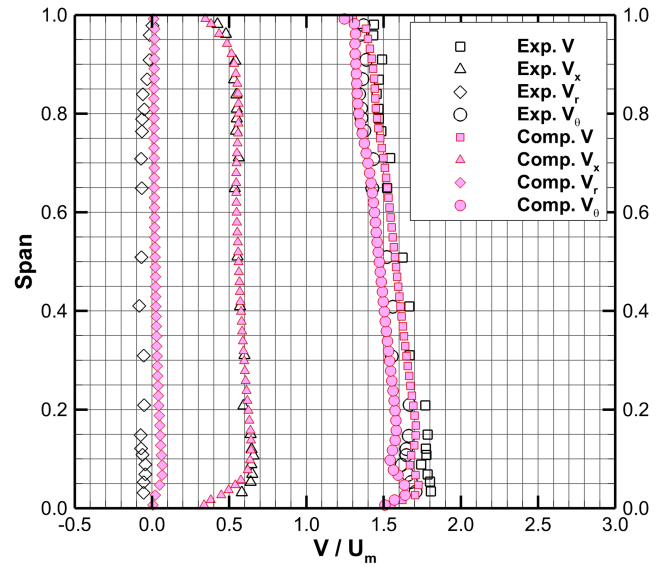
(a) Frozen rotor without rim seal flow

(b) Frozen rotor with 0.75% rim seal flow

**FIGURE 11:** Contour lines of  $C_{P_t}$  at rotor inlet plane with and without rim seal flow.



(a) Pressure coefficient



(b) Velocity components

**FIGURE 12:** The distribution of pressure coefficient and velocity components at NGV exit plane with 0.75% rim seal flow, comparison with experimental data [21].

sure coefficient and the velocity components below 30% span. Note that, the comparison between Figs. 12a and 8a tells that below 10%,  $C_P$  deviates from experimental data more in the case

with rim seal flow. This static pressure rise, closer to the endwall at the NGV exit, is in accordance with Schuepbach et al. [18]. The increase in the static pressure is mainly due to the existence

of the blockage created by the rim seal flow. And accordingly, the velocity magnitudes decrease closer to the hub endwall.

## CONCLUSIONS

The 3D viscous flow through an axial turbine stage has been simulated and compared to the experimental measurements. The axial flow turbine facility has 23 vanes and 29 blades, which indicates that the pitch ratio between the components is approximately 1.25. For accurate rotor-stator CFD simulations, it is suggested to make this ratio closer to unity. The authors tried two different ways to bring down the ratio close to unity. First way was to scale the rotor blade such that there would be 23 of them in the rotating domain. The second way was using 4 vanes and 5 blades in the simulation. The comparison of the total pressure coefficient distribution at the NGV exit and the rotor inlet plane showed that the results for the two methods were close to each other. Then, the authors carried on with the blade scaling technique for computational time and resource considerations.

The three types of rotor-stator interface models were tested, frozen rotor, stage, and transient rotor-stator model. Even though the stage model lacks the transient effects, it successfully simulated the time-averaged rotor-stator interaction. The results were in good agreement with the ones coming from time-averaged transient model at the NGV exit and rotor inlet plane.

The comparison of NGV only simulation and the rotor-stator simulation showed that the peak value of  $C_{P_i}$  decreased by 13% for the rotor included case at the rotor inlet plane. Also, the location of the secondary flow core moved 2.5% in the radially upward direction. Still, there was a mismatch between the experimental measurement and the computational evaluations.

The rim seal flow between the stationary and the rotating domains was simulated to deal with this mismatch. Various seal flow rates has been tested, and among them, 0.75% of the mainstream flow rate gave reasonably agreeing results with the experimental data. As the seal mass flow rate was increased, the location of the secondary flow area moved upwards in the spanwise direction at the NGV exit plane. And, the peak value of the secondary flow was reduced. These observations was also valid at the rotor inlet plane.

The endwall boundary layer height occupies 1.5% span for the case without seal flow, whereas, when the seal flow was introduced this number went up to 6% span. Another observation was the magnitude of the secondary flow core did not change with the seal flow. However, the secondary flow location moved from 8% pspan location to 11% span.

## ACKNOWLEDGMENT

The authors acknowledge the financial support provided by the Siemens Energy Inc. and thank to Dr. Matthew Montgomery, Dr. Prakash Chander, Dr. Michael Crawford, Andrew Lohaus,

Anthony Malandra, Ching-Pang Lee, Boris Dobrzynski, Humberto Zuniga, Ken Landis, and Dirk Nuernberger. The authors are thankful to Dr. Ali Aktürk for his support during this study. The authors are also indebted to Dr. Peter R. Eiseman of Program Development Company, LLC for his great help in grid development for our study.

## REFERENCES

- [1] Johnson, B. V., Mack, G. J., Paolillo, R. E., and Daniels, W. A., 1994. "Turbine Rim Seal Gas Path Flow Ingestion Mechanisms". *AIAA Paper No. AIAA94-2703*.
- [2] Kobayashi, N., Matsumoto, M., and Shizuya, M., 1984. "An Experimental Investigation of a Gas Turbine Disk Cooling System". *ASME Journal of Engineering for Gas Turbines and Power*, **106**, pp. 136–141.
- [3] Chew, J. W., Dadkhah, S., and Turner, A. B., 1992. "Rim Sealing of Rotor-Stator Wheelspaces in the Absence of External Flow". *ASME Journal of Turbomachinery*, **114**, pp. 433–438.
- [4] Dadkhah, S., Turner, A. B., and Chew, J. W., 1992. "Performance of Radial Clearance Rim Seals in Upstream and Downstream Rotor-Stator Wheelspaces". *ASME Journal of Turbomachinery*, **114**, pp. 439–445.
- [5] Förster, I., Martens, E., Friedl, W.-H., and Peitsch, D., 2001. "Numerical Study of Hot Gas Ingestion into an Engine Type High-Pressure Turbine Rotor-Stator Cavity". *ASME Paper No. 2001-GT-114*.
- [6] Cao, C., Chew, J. W., Millington, P. R., and Hogg, S. I., 2004. "Interaction of Rim Seal and Annulus Flows in an Axial Flow Turbine". *ASME Journal of Engineering for Gas Turbines and Power*, **126**, pp. 786–793.
- [7] Jakoby, R., Zierer, T., Lindblad, K., Larsson, J., deVito, L., Bohn, D. E., Funcke, J., and Decker, A., 2004. "Numerical Simulation of the Unsteady Flow Field in an Axial Gas Turbine Rim Seal Configuration". *ASME Paper No. GT2004-53829*.
- [8] Johnson, B. V., Jakoby, R., Bohn, D. E., and Cunat, D., 2009. "A Method for Estimating the Influence of Time-Dependent Vane and Blade Pressure Fields on Turbine Rim Seal Ingestion". *ASME Journal of Turbomachinery*, **131**, p. 021005.
- [9] Bunker, R. S., Laskowski, G. M., Bailey, J. C., Palafox, P., Kapetanovic, S., Itzel, G. M., Sullivan, M. A., and Farrell, T. R., 2011. "An Investigation of Turbine Wheel-space Cooling Flow Interactions With a Transonic Hot Gas Path—Part 1: Experimental Measurements". *ASME Journal of Turbomachinery*, **133**, p. 021015.
- [10] Hunter, S. D., and Manwaring, S. R., 2000. "Endwall Cavity Flow Effects on Gaspath Aerodynamics in an Axial Flow Turbine: Part I Experimental and Numerical Investigation". *ASME Paper No. 2000-GT-651*.

- [11] McLean, C., Camcı, C., and Glezer, B., 2001. "Mainstream Aerodynamic Effects Due to Wheel-space Coolant Injection in a High-Pressure Turbine Stage: Part I - Aerodynamic Measurements in the Stationary Frame". *ASME Journal of Turbomachinery*, **123**, pp. 687–696.
- [12] McLean, C., Camcı, C., and Glezer, B., 2001. "Mainstream Aerodynamic Effects Due to Wheel-space Coolant Injection in a High-Pressure Turbine Stage: Part II - Aerodynamic Measurements in the Rotational Frame". *ASME Journal of Turbomachinery*, **123**, pp. 697–703.
- [13] Paniagua, G., Déno, R., and Almeida, S., 2004. "Effect of the Hub Endwall Cavity Flow on the Flow-Field of a Transonic High-Pressure Turbine". *ASME Journal of Turbomachinery*, **126**, pp. 578–586.
- [14] Gallier, K. D., Lawless, P. B., and Fleeter, S., 2004. "Development of the Unsteady Flow on a Turbine Rotor Platform Downstream of a Rim Seal". *ASME Paper No. GT2004-53899*.
- [15] Ong, J. H. P., Miller, R. J., and Uchida, S., 2006. "The Effect of Coolant Injection on the Endwall Flow of a High Pressure Turbine". *ASME Paper No. GT2006-91060*.
- [16] Reid, K., Denton, J., Pullan, G., Curtis, E., and Longley, J., 2006. "The Effect of Stator-Rotor Hub Sealing Flow on the Mainstream Aerodynamics of a Turbine". *ASME Paper No. GT2006-90838*.
- [17] Schuepbach, P., Abhari, R. S., Rose, M. G., Germain, T., Raab, I., and Gier, J., 2010. "Effects of Suction and Injection Purge-Flow on the Secondary Flow Structures of a High-Work Turbine". *ASME Journal of Turbomachinery*, **132**, p. 021021.
- [18] Schuepbach, P., Abhari, R. S., Rose, M. G., and Gier, J., 2011. "Influence of Rim Seal Purge Flow on the Performance of an Endwall-Profiled Axial Turbine". *ASME Journal of Turbomachinery*, **133**, p. 021011.
- [19] Turgut, Ö. H., and Camcı, C., 2011. "A Computational Validation of Turbine Nozzle Guide Vane Aerodynamic Experiments in an HP Turbine Stage". *ASME Paper No. IMECE2011-64352*.
- [20] Camcı, C., 2004. "Experimental and Computational Methodology for Turbine Tip De-sensitization". *VKI Lecture Series 2004-02, Turbine Blade Tip Design and Tip Clearance Treatment*.
- [21] Zaccaria, M., and Lakshminarayana, B., 1995. "Investigation of Three-Dimensional Flowfield at the Exit of a Turbine Nozzle". *Journal of Propulsion and Power*, **11**(1), January-February, pp. 55–63.
- [22] United Sensor Corporation, Kiel Probes. URL: <http://www.unitedsensorcorp.com/kiel.html>.
- [23] Zaccaria, M. A., 1994. "An Experimental Investigation Into the Steady and Unsteady Flow Field in an Axial Flow Turbine". PhD Thesis, The Pennsylvania State University, University Park, PA.
- [24] Michelassi, V., Martelli, F., Déno, R., Arts, T., and Sieverding, C. H., 1999. "Unsteady Heat Transfer in Stator-Rotor Interaction by Two-Equation Turbulence Model". *ASME Journal of Turbomachinery*, **121**, pp. 436–447.
- [25] Ameri, A. A., Rigby, D. L., Heidmann, J., Steinthorsson, E., and Fabian, J. C., 2008. "Unsteady Analysis of Blade and Tip Heat Transfer as Influenced by the Upstream Momentum and Thermal Wakes". *ASME Paper No. GT2008-51242*.
- [26] Dawes, W. N., 1994. "A Numerical Study of the Interaction of a Transonic Compressor Rotor Overtip Leakage Vortex with the Following Stator Blade Row". *ASME Paper No. 94-GT-156*.
- [27] Ameri, A. A., Rigby, D. L., Steinthorsson, E., Heidmann, J., and Fabian, J. C., 2007. "Numerical Simulation of Unsteady Turbine Blade and Tip Heat Transfer Due To Wake Passing". *ASME Paper No. GT2007-27550*.
- [28] Abhari, R. S., Guenette, G. R., Epstein, A. H., and Giles, M. B., 1992. "Comparison of Time-Resolved Turbine Rotor Blade Heat Transfer Measurements and Numerical Calculations". *ASME Journal of Turbomachinery*, **114**, pp. 818–827.
- [29] He, L., and Denton, J. D., 1994. "Three-Dimensional Time-Marching Inviscid and Viscous Solutions for Unsteady Flows Around Vibrating Blades". *ASME Journal of Turbomachinery*, **116**, pp. 469–476.
- [30] Gerolymos, G. A., Michon, G. J., and Neubauer, J., 2002. "Analysis and Application of Chorochnic Periodicity in Turbomachinery Rotor/Stator Interaction Computations". *Journal of Propulsion and Power*, **18**(6), November-December, pp. 1139–1152.
- [31] D. Van Z., Chen, J., Hathaway, M., and Chriss, R., 2008. "The Influence of Compressor Blade Row Interaction Modeling on Performance Estimates From Time-Accurate, Multistage, Navier-Stokes Simulations". *ASME Journal of Turbomachinery*, **130**, p. 011009.
- [32] Shyam, V., Ameri, A., Luk, D. F., and Chen, J.-P., 2011. "3D Unsteady Simulation of a Modern High Pressure Turbine Stage Using Phase Lag Periodicity: Analysis of Flow and Heat Transfer". *ASME Journal of Turbomachinery*, **133**, p. 031015.
- [33] Giles, M. B., 1990. "Rotor/Stator Interaction in a Transonic Turbine". *Journal of Propulsion and Power*, **6**(5), September-October, pp. 621–627.
- [34] Jung, A. R., Mayer, J. F., and Stetter, H., 1996. "Simulation of 3D-Unsteady Stator/Rotor Interaction in Turbomachinery Stages of Arbitrary Pitch Ratio". *ASME Paper No. 96-GT-69*.
- [35] Zhou, L., Xi, G., and Cai, Y. H., 2007. "Unsteady Numerical Simulation in a Centrifugal Compressor Using the Time-Inclined Operator". *Proc. IMechE Part G: J. of Aerospace Engineering*, **221**(5), pp. 795–804.

[36] Menter, F. R., 1994. "Two-Equation Eddy-Viscosity Turbulence Models for Engineering Applications". *AIAA Journal*, 32(8), pp. 1598–1605.

## Appendix A: Methods used for unequal blade count ratio

As discussed in the previous sections, the pitch ratio between the stationary domain and the rotating domain is around 1.25, which would influence the accuracy of the rotor-stator simulation at the interface. It is suggested to have this ratio close to one, and to make this ratio as close as possible to unity, the authors of this paper tested two different approach. The first one is to scale the blade such that the pitch ratio is equal to one. The other method is to use 4 vanes and 5 blades. These methods are compared based on total pressure coefficient distribution at NGV exit plane and rotor inlet plane, as shown in Figs. 13 and 14. The  $C_{Pt}'$  distributions at NGV exit are similar to each other for these two methods along the span except the region near the hub end-wall. Similarly, the  $C_{Pt}$  distribution in Fig. 14 shows that scaling the blade predict the total pressure in accordance to the 4 vanes 5 blades computation. The scaled rotor simulation deviates from the other method below 7% span. The maximum deviation is found to be 10% at 5% span. Note that, at both planes, these two methods estimate the total pressure loss almost the same at the secondary flow area and the wake region. Even though there is a mismatch near the hub endwall, it may be concluded that scaling the rotor blade in the AFTRF simulation did not create significant aerodynamic loss.

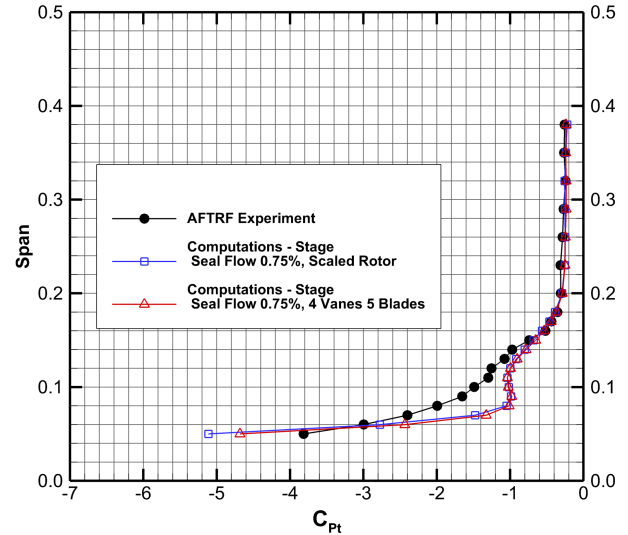


**FIGURE 14:** Total pressure coefficient distribution at rotor inlet plane.

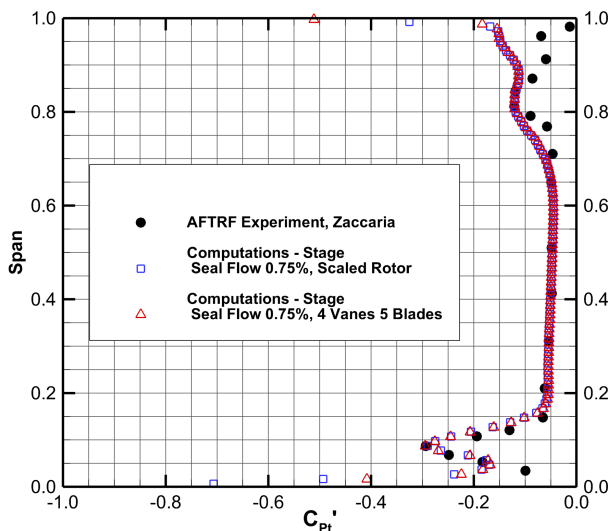


**FIGURE 13:** Total pressure coefficient distribution at NGV exit plane, compared with experimental data [21].